

The anisotropic quasi-static permittivity of single-crystal β -Ga₂O₃ measured by terahertz spectroscopy ^{EP}

Cite as: Appl. Phys. Lett. **117**, 252103 (2020); <https://doi.org/10.1063/5.0031464>

Submitted: 30 September 2020 . Accepted: 01 December 2020 . Published Online: 21 December 2020

^{ID} Prashanth Gopalan, ^{ID} Sean Knight, ^{ID} Ashish Chanana, ^{ID} Megan Stokey, ^{ID} Praneeth Ranga, ^{ID} Michael A. Scarpulla, ^{ID} Sriram Krishnamoorthy, ^{ID} Vanya Darakchieva, ^{ID} Zbigniew Galazka, ^{ID} Klaus Irmischer, ^{ID} Andreas Fiedler, Steve Blair, ^{ID} Mathias Schubert, and Berardi Sensale-Rodriguez

COLLECTIONS

Note: This paper is part of the Special Topic on Ultrawide Bandgap Semiconductors.

^{EP} This paper was selected as an Editor's Pick



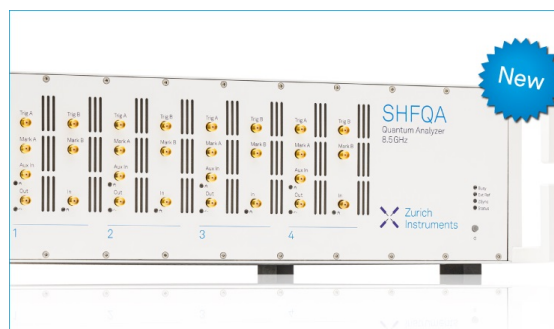
View Online



Export Citation



CrossMark



Your Qubits. Measured.

Meet the next generation of quantum analyzers

- Readout for up to 64 qubits
- Operation at up to 8.5 GHz, mixer-calibration-free
- Signal optimization with minimal latency

Find out more

 Zurich Instruments

The anisotropic quasi-static permittivity of single-crystal β -Ga₂O₃ measured by terahertz spectroscopy

Cite as: Appl. Phys. Lett. **117**, 252103 (2020); doi: [10.1063/5.0031464](https://doi.org/10.1063/5.0031464)

Submitted: 30 September 2020 · Accepted: 1 December 2020 ·

Published Online: 21 December 2020

















View Online



Export Citation



CrossMark

Prashanth Gopalan,¹  Sean Knight,²  Ashish Chanana,¹  Megan Stokey,³  Praneeth Ranga,¹  Michael A. Scarpulla,^{1,4}  Sriram Krishnamoorthy,¹  Vanya Darakchieva,²  Zbigniew Galazka,⁵  Klaus Imscher,⁵  Andreas Fiedler,⁵  Steve Blair,¹  Mathias Schubert,^{2,3,6}  and Berardi Sensale-Rodriguez^{1,a)} 

AFFILIATIONS

¹Department of Electrical and Computer Engineering, The University of Utah, Salt Lake City, Utah 84112, USA

²Terahertz Materials Analysis Center and Competence Center for III-Nitride Technology C3NIT-Janzén, Department of Physics, Chemistry and Biology (IFM), Linköping University, Linköping SE 58183, Sweden

³Department of Electrical and Computer Engineering, University of Nebraska-Lincoln, Lincoln, Nebraska 68588, USA

⁴Department of Material Science and Engineering, The University of Utah, Salt Lake City, Utah 84112, USA

⁵Leibniz-Institut für Kristallzüchtung, Berlin, e.V., Berlin 12489, Germany

⁶Leibniz Institut für Polymerforschung e.V., 01069 Dresden, Germany

Note: This paper is part of the Special Topic on Ultrawide Bandgap Semiconductors.

a) Author to whom correspondence should be addressed: berardi.sensale@utah.edu

ABSTRACT

The quasi-static anisotropic permittivity parameters of electrically insulating beta gallium oxide (β -Ga₂O₃) were determined by terahertz spectroscopy. Polarization-resolved frequency domain spectroscopy in the spectral range from 200 GHz to 1 THz was carried out on bulk crystals along different orientations. Principal directions for permittivity were determined along crystallographic axes **c** and **b** and reciprocal lattice direction **a***. No significant frequency dispersion in the real part of dielectric permittivity was observed in the measured spectral range. Our results are in excellent agreement with recent radio frequency capacitance measurements as well as with extrapolations from recent infrared measurements of phonon mode and high-frequency contributions and close the knowledge gap for these parameters in the terahertz spectral range. Our results are important for applications of β -Ga₂O₃ in high-frequency electronic devices.

Published under license by AIP Publishing. <https://doi.org/10.1063/5.0031464>

Single crystalline monoclinic structure beta gallium oxide (β -Ga₂O₃), an ultra-wide bandgap semiconductor with the direct bandgap reported in the range from 4.8 eV to 5.04 eV,^{1–6} is being extensively researched due to its potential for improved performance in a wide variety of power switching applications as well as radio frequency (RF) components typically employed in power supplies, radar, communication systems, etc.⁷ Because of its high estimated breakdown field (E_{br}) of approximately 6–8 MV/cm,^{8–10} its Baliga figure of merit, which is proportional to the third power of E_{br} , has been estimated to be greater than that of Si and GaN.^{8,11} In addition to this primary area of application, since its optical absorption edge lies at ultra-violet (UV) wavelengths, β -Ga₂O₃ may also potentially enable the development of solar-blind UV optoelectronic devices.^{12,13} Moreover, a large bandgap energy and controllable *n*-type doping

could also facilitate its use as a transparent conductive film for deep-UV applications.^{1,14} While the overall focus of β -Ga₂O₃ research is targeted toward electronic device applications, there is a considerable need to understand its dielectric permittivity $\bar{\epsilon}(\omega)$ at different frequencies from static (DC), through the far infrared (FIR) and infrared (IR) to the visible, ultraviolet (UV), and deep ultraviolet (DUV) spectral regions.^{2,3,5,15–18} As a fundamental constitutive material parameter, the permittivity is a direct measure of the polarizability of the constituent atomic lattice and the electron charge distribution under an externally applied electric field. The low symmetry (*C*₂/m) of monoclinic β -Ga₂O₃ results in strongly anisotropic dielectric permittivity parameters along different crystal directions. This anisotropic behavior extends over different frequency regions and, hence, requires comprehensive characterization. Recently, FIR and IR ellipsometric

measurements have identified transverse (TO) and longitudinal (LO) phonon mode parameters and their contributions to the anisotropic permittivity in the FIR–IR spectral region. It was observed that phonons polarized within the monoclinic plane do not coincide with specific crystallographic directions, and as a consequence, TO and LO phonons do not coincide in the polarization direction either.^{16,19–22} A generalization of the well-known Lyddane–Sachs–Teller relationship was reported for monoclinic and triclinic materials, which relate static and high-frequency permittivity values to the infrared-active phonon mode parameters.^{16,23} More recently, Fiedler *et al.* using AC measurements on capacitor structures fabricated perpendicular to principal planes (100), (010), and (001) reported strong anisotropy of the measured permittivity.¹⁵ However, in low-symmetry crystal systems, principal lattice planes are not perpendicular to principal unit cell directions, and the AC capacitance measurements did not provide the full set of intrinsic permittivity values. In this Letter, we characterize the quasi-static dielectric permittivity of β -Ga₂O₃ in the frequency range approximately from 0.2 to 1 THz, and we obtain the full set of permittivity values for all major lattice directions and directions perpendicular to all principal planes. We compare our results with those from AC capacitance and FIR–IR spectral investigations. Our investigation bridges the previously reported FIR–IR and AC capacitance studies and provides information about the dielectric permittivity in the upper gigahertz spectral region of this emerging semiconductor.

Due to the monoclinic symmetry, the anisotropy of β -Ga₂O₃ requires careful consideration of lattice directions and unambiguous assignment of lattice axes and coordinate systems. In general, the dielectric tensor possesses four independent complex-valued elements and cannot be diagonalized for all wavelengths due to the frequency dependence of the permittivity. Optical axes, which describe directions within a given crystal along which light can propagate while maintaining its polarization, change angular orientation in spectral regions where the permittivity undergoes dispersion in monoclinic crystal systems. This phenomenon is also known as rotation of optical axes. This was recently demonstrated for the IR and FIR range for β -Ga₂O₃, where all four tensor components show strong dispersion behavior across the phonon mode spectral region.¹⁶ In another example, Yiwen *et al.* studied propagation of terahertz waves in a monoclinic crystal of BaGa₄Se₇.²⁴ The existence of free charge carriers with direction-dependent mobility parameters produces anisotropic properties with strong dispersion in the terahertz spectral range. If free charge carriers can be suppressed, either by compensation doping or by using high-quality crystalline material, then the dielectric response is composed of all higher frequency bound excitations, such as phonons, band-to-band transitions, excitons, and x-ray absorption. Phonon modes in this material system are known to be present at frequencies >3 THz.^{16,25,26} If phonon modes are far enough away from the terahertz spectral range measured, then the dispersion caused by phonons can be neglected. If there is no other dielectric mechanism such as polaron absorption or charge re-localization between different defects, then the dielectric permittivity tensor should be constant and reveal no significant frequency dispersion. This criterion is important for determining dielectric constants, which can then be compared with static or AC measurements. We, therefore, refer to the terahertz dielectric permittivity parameters here discussed as quasi-static permittivity parameters. We use polarization-resolved frequency domain spectroscopy methods and extract the anisotropic dielectric permittivity along

different crystal directions. We compare our results with recent AC capacitance measurements as well as with extrapolations from recent FIR–IR measurements of phonon mode and high frequency permittivity contributions, which close the knowledge gap for these parameters in the terahertz spectral range. The results of our study are of great technological interest for applications of β -Ga₂O₃ in electronic devices.

Figure 1 depicts the unit cell of β -Ga₂O₃ and a set of Cartesian coordinates (x, y, z), which represent the laboratory coordinates that are permanently assigned to the monoclinic system (a, b, c) as depicted in Fig. 1(b). Euler rotations then relate these laboratory coordinates to the auxiliary (or the ellipsometer) coordinate system (x', y', z'), which, in turn, represents the respective surface cut and sample rotation for every measurement (as explained in more detail in Ref. 16). Due to the monoclinic angle ($\beta = 103.7^\circ$),²⁷ axes a and c are not perpendicular to each other. The samples investigated in this work are characterized by the Miller indices of the crystallographic planes at the surface. The vectors normal to the planes are obtained by the reciprocal lattice vectors,

$$\mathbf{a}^* = \frac{\mathbf{b} \times \mathbf{c}}{\mathbf{a}(\mathbf{b} \times \mathbf{c})}, \quad \mathbf{b}^* = \frac{\mathbf{a} \times \mathbf{c}}{\mathbf{b}(\mathbf{a} \times \mathbf{c})}, \quad \mathbf{c}^* = \frac{\mathbf{a} \times \mathbf{b}}{\mathbf{c}(\mathbf{a} \times \mathbf{b})}, \quad (1)$$

where \times is the vector product, and because \mathbf{b} is perpendicular to \mathbf{a} and \mathbf{c} , vectors \mathbf{b}^* and \mathbf{b} are parallel. Vectors \mathbf{a}^* and \mathbf{c}^* are depicted in Fig. 1(b).

The frequency-dependent permittivity of β -Ga₂O₃ can be expressed by a second-rank tensor,¹⁶

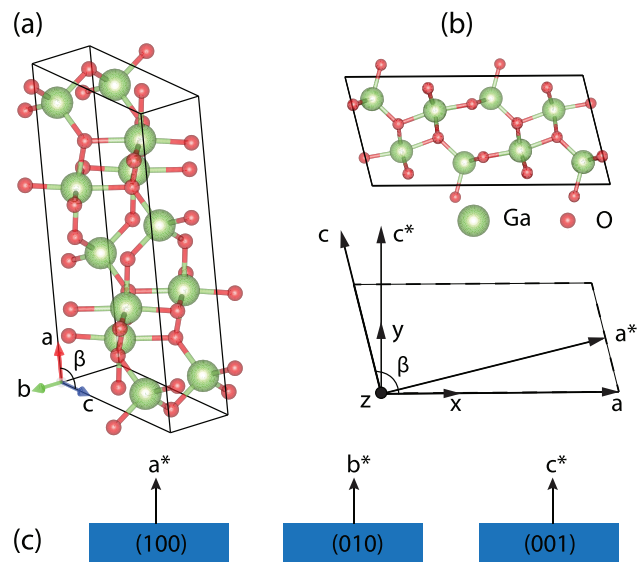


FIG. 1. (a) The unit cell of β -Ga₂O₃ with monoclinic angle β and crystal unit axes a , b , and c . (b) Monoclinic plane a - c viewed along axis b (b points into the plane). Definition of the laboratory Cartesian coordinate system (x, y, z) and crystal unit axes (a, b, c). Reciprocal lattice vector \mathbf{c}^* parallel to axis y , \mathbf{a}^* parallel to axis x , and \mathbf{b}^* parallel to axis z (not drawn to scale). Principal plane Miller indices for surfaces of samples investigated here are shown in (c), with surface normal reciprocal lattice vectors. Note that $\mathbf{b}^* \parallel \mathbf{b}$. The relationship between the laboratory coordinate system (x, y, z) and the monoclinic system (a, b, c) shown in (b) is valid for all surface orientations shown in (c). The figure was redrawn with permission from Phys. Rev. B 93, 125209 (2016).¹⁶ Copyright 2016 American Physical Society.

$$\bar{\epsilon}(\omega) = \begin{bmatrix} \epsilon_{xx} & \epsilon_{xy} & 0 \\ \epsilon_{xy} & \epsilon_{yy} & 0 \\ 0 & 0 & \epsilon_{zz} \end{bmatrix}, \quad (2)$$

where elements ϵ_{xx} , ϵ_{xy} , ϵ_{yy} , and ϵ_{zz} are generally independent functions of frequency. With the coordinates defined in Fig. 1, ϵ_{xx} , ϵ_{yy} , and ϵ_{zz} correspond to permittivities for displacements occurring along axes **a**, **c**^{*}, and **b**, respectively, while ϵ_{xy} corresponds to the shear contribution due to displacements occurring along directions *y* under electric fields along *x* and vice versa. Simple Euler angle rotations around axes *z* (ϕ), *x* (θ), and *z'* (ψ ; axis *z* after rotation by θ) as defined in Ref. 16 permit us to express the permittivity tensor in the coordinate system (*x'*, *y'*, *z'*) of the measurement setup and according to the crystallographic surface orientation of a given sample. For example, rotation of $\bar{\epsilon}$ in Eq. (2) by $\phi = -(\beta - 90^\circ)$ results in new elements $\epsilon_{x'x'}$ and $\epsilon_{y'y'}$, which correspond to permittivity parameters for displacements occurring along axes **a**^{*} and **c**, respectively. We determine the anisotropy and the frequency-dependent permittivity tensor by frequency-domain polarized terahertz transmission measurements (THz-pT) at normal incidence and generalized spectroscopic ellipsometry (THz-GSE) at the oblique angle of incidence in reflection.

We use the Mueller matrix concept²⁸ to describe the electromagnetic properties of an arbitrary anisotropic sample, represented by its input Stokes vector into its outgoing Stokes vector,

$$\begin{pmatrix} S_0 \\ S_1 \\ S_2 \\ S_3 \end{pmatrix}_{\text{output}} = \begin{pmatrix} M_{11} & M_{12} & M_{13} & M_{14} \\ M_{21} & M_{22} & M_{23} & M_{24} \\ M_{31} & M_{32} & M_{33} & M_{34} \\ M_{41} & M_{42} & M_{43} & M_{44} \end{pmatrix} \begin{pmatrix} S_0 \\ S_1 \\ S_2 \\ S_3 \end{pmatrix}_{\text{input}}, \quad (3)$$

with Stokes vector components defined here by $S_0 = I_p + I_s$, $S_1 = I_p - I_s$, $S_2 = I_{45} - I_{-45}$, $S_3 = I_+ - I_-$, and I_p , I_s , I_{45} , I_{-45} , I_+ , and I_- denote the intensities for the *p*-, *s*-, $+45^\circ$, -45° , left-handed, and right-handed circularly polarized light components, respectively.^{29,30} In our THz-GSE setup,³¹ we obtain elements in the upper 3×3 block normalized to element M_{11} . We use matrix algebra approaches to calculate the Mueller matrix elements for arbitrary anisotropic permittivity configurations, as explained in detail previously.^{5,16,19,29,32} In THz-pT, we measure $M_{11} + M_{12}$, which corresponds to the linearly polarized (horizontal) Stokes vector intensity.

Three electrically insulating samples were studied in our measurements; (i) sample A—Czochralski-grown Al^{3+} -doped crystal with (100) surface orientation,^{33,34} (ii) sample B—(010) Fe-doped crystal, and (iii) sample C—Fe-doped (001) substrate (refer to the supplementary material for additional details). The thickness parameters of all samples were determined by mechanical measurements and from analysis of the spectroscopic measurements (in good agreement with each other). Crystallographic plane Miller indices for surfaces of samples investigated here are shown in Fig. 1(c), with surface normal vectors expressed in reciprocal lattice vectors.

THz-GSE measurements were carried out at angles of incidence of 40° and 60° in a reflection configuration on sample A and sample B, wherein the samples were also rotated to multiple azimuth orientations as described in Ref. 16. THz-GSE data from these samples were analyzed simultaneously in a best-match model regression analysis to determine the values of the relevant permittivity tensor elements. Specific sample orientations were accounted for by mathematical rotations of the permittivity tensor. THz-pT measurements were

performed on samples B and C using a linearly polarized incident beam at normal incidence. Samples were oriented such that the incident electric field is parallel to **a**^{*}, **b**, and **c** axes.

Figure 2 depicts the selected reflection-type GSE data from sample A, (100) β - Ga_2O_3 , at multiple angles of incidence and at multiple sample azimuths. Experimental data and best-match model calculated data are in excellent agreement. Upon rotation to various azimuths, the sample reveals strong anisotropy, recognizable in nonvanishing off-diagonal block elements M_{31} , M_{13} , M_{32} , and M_{23} . At azimuth positions P1 and P3, axes **b** and **c** align with the instrument coordinates *x* and *y*, and therefore, the off-diagonal block elements vanish. Similar data are shown in the supplementary material for sample B. Both datasets were analyzed simultaneously, where parameters for $\bar{\epsilon}$ and azimuth orientation ϕ are determined. Our analysis reveals that the fourth tensor element ϵ_{xy} is too small to be identified. This observation is in agreement with our previous IR-FIR GSE results where the DC value of ϵ_{xy} was predicted by extrapolation to be very small (-0.13).¹⁶ Hence, in the measured frequency range, we find that the permittivity tensor can be diagonalized, where only three elements are needed. These three elements correspond to the principal dielectric axes. An excellent match to the measured Mueller matrix data can be achieved by setting the directions of the principal axes to be along **a**^{*}, **b**, and **c**. Therefore, the Euler angles for the (100) cut sample A are fixed at $\theta = 90^\circ$ and $\psi = 90^\circ$ and for (010) cut sample B at $\theta = 0^\circ$ and $\psi = 0^\circ$. We note that the principal dielectric axis directions in monoclinic materials do not necessarily coincide with crystallographic axes. For the case of β - Ga_2O_3 , we find that these axes are indistinguishably close to **a**^{*}, **b**, and **c**. This observation is further verified by the THz-pT measurements as discussed below. Furthermore, we observe no dispersion in the measured frequency range (0.6–0.9 THz). From the frequency-independent values of $\bar{\epsilon}$, permittivity parameters for all crystallographic axes are obtained and listed in Table I.

Figures 3(a) and 3(b) depicts THz-pT data for sample B, (010) β - Ga_2O_3 , while Fig. 3(c) shows the THz-pT data for sample C, (001) β - Ga_2O_3 . In order to obtain the data shown in Figs. 3(a) and 3(b), the orientation of sample B was rotated with respect to the polarization of the incident terahertz beam and the corresponding transmission was measured at several angles in the **a**–**c** plane. We expect to observe single-mode Fabry–Pérot (FP) oscillations when the incident E-field is along a major polarizability axis, and given the insulating nature of the Fe-doped substrates, we expect the FP transmission maxima to approach unity. Our measurement of polarization-resolved transmission at different angles in the **a**–**c** plane indicates that the principal axes are close to **a**^{*} and **c**-directions in the (010) substrate (in agreement with the THz-GSE results). Figures 3(a) and 3(b) show the transmitted E-field amplitude when the directions **a**^{*} and **c** are aligned with the incident polarization, respectively. Figure 3(c) shows the THz-pT data for sample C where the in-plane **b** axis is parallel to the incident polarization. Experimental data and best-match model are in good agreement (see the supplementary material for further details). The indices of refraction values extracted from these particular analyses are $n_{a^*} = 3.16 \pm 0.09$, $n_c = 3.51 \pm 0.10$, and $n_b = 3.18 \pm 0.035$. No frequency dispersion is observed as evidenced by a constant free spectral range over the measured spectral range. A small drop of the peak transmission levels is observed at the higher frequency end of the measured spectrum (i.e., above 0.7 THz), which, in all cases, is associated with an imaginary part of refractive index $\ll 0.01$.

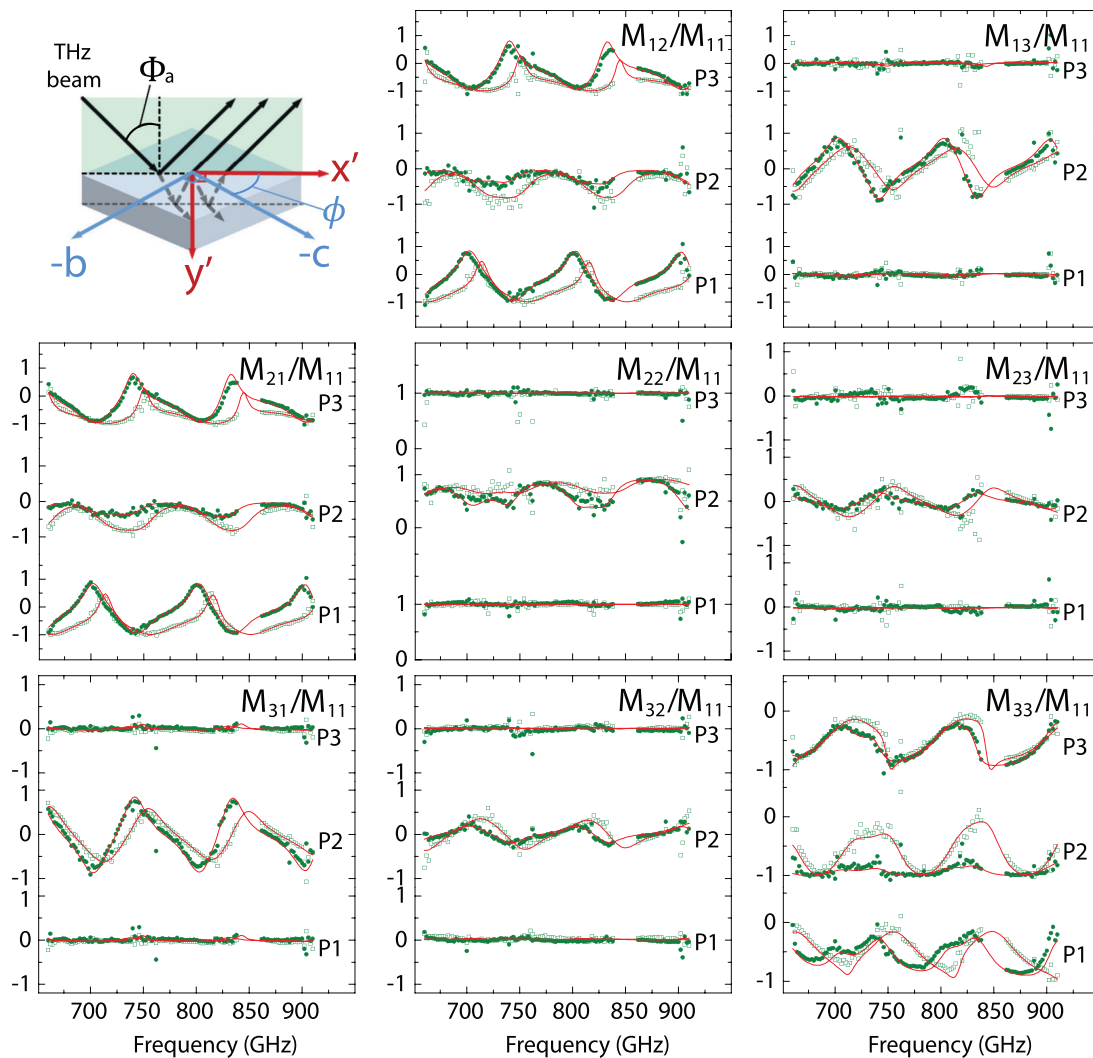


FIG. 2. GSE data of sample A, (100) β -Ga₂O₃, at angles of incidence of $\Phi_a = 40^\circ$ and 60° : green symbols (experiment); solid red lines (best match model calculated). Solid green circles indicate data for $\Phi_a = 40^\circ$, and open squares for $\Phi_a = 60^\circ$. Data are presented in the Mueller matrix formalism. All data are normalized to element M_{11} . Data are shown for three azimuths: P1 ($\varphi = -1.5^\circ \pm 0.2^\circ$); P2 ($\varphi = 43.5^\circ \pm 0.2^\circ$); P3 ($\varphi = 88.5^\circ \pm 0.2^\circ$). The inset depicts schematically the location of axes **b** and **c** in position P2. Axes x' and y' indicate the ellipsometer coordinate axes, where x' and z' are parallel to the plane of incidence. The sample thickness was determined from the same model analysis as $d = 469 \pm 1 \mu\text{m}$.

All permittivity values obtained here are listed in Table I and compared with previous AC capacitance and FIR investigation results. Our results are consistent across our two techniques and compare very well with the previous electrical and optical methods. It is worth noticing that the error bars for the THz-GSE results are significantly smaller compared to the THz-pT results. This is a result of (i) more information about the samples' optical response being contained in the Mueller matrix spectra in comparison to the measured transmission spectra and (ii) the Mueller matrix analysis being performed on a dataset that contains information from two samples (A and B) measured at multiple incident angles and sample azimuths. In comparison, THz-pT data for \mathbf{a}^* and \mathbf{c}^* are obtained at normal incidence and a few in-plane angles (from

sample B only), while the value along the **b** axis is obtained from sample C when the incident E-field is parallel to **b**. The AC capacitance measurements report permittivity values that correspond to the reciprocal directions of the principal lattice planes, i.e., \mathbf{a}^* , \mathbf{b}^* , and \mathbf{c}^* corresponding to (100), (010), and (001) planes, respectively. Some of us reported previously on an FIR-IR GSE analysis by introducing a parameterized eigendielectric polarization model for phonon mode contributions based on a best-match model of the four functions of the permittivity tensor. From the extrapolation in this model toward zero frequency, the DC permittivity values were reported. It is noted here that due to a misprint, values reported in Ref. 16 for permittivity parameters corresponding to **a** and **c** were accidentally switched and are reported correctly here.

TABLE I. Static permittivity parameters for β -Ga₂O₃ for dielectric displacement along axes **a**, **a***, **b**, **c**, and **c*** as defined in Fig. 1, obtained from THz-GSE and THz-pT experiments, in comparison with theory, AC capacitance measurements, and extrapolations from FIR-IR GSE using the eigendielectric polarization model. Note that the values given for the THz-GSE-determined **a** and **c*** are calculated by rotating the diagonalized permittivity tensor (which contains the values of **a***, **b**, and **c**). Error bars indicate the confidence interval at 95% confidence level. For the FIR-IR GSE results from Ref. 16, the last digit, which is determined at the 90% confidence level, is indicated within the parentheses.

	a	c*	a*	c	b
THz-GSE	10.19 ^a	12.27 ^a	10.05 ± 0.05	12.4 ± 0.06	10.6 ± 0.06
THz-pT	10.11 ^b	12.21 ^b	9.97 ± 0.57	12.35 ± 0.70	10.09 ± 0.23
AC capacitance ¹⁵	...	12.4 ± 0.04	10.2 ± 0.2	...	10.87 ± 0.08
FIR-IR GSE ¹⁶	10.(9)	12.(7)	10.(8)	12.(6)	11.(2)
Theory ³⁵	10.84	13.89	11.49

^aThe resulting off-diagonal tensor component associated with **a** and **c*** is -0.54 .

^bThe resulting off-diagonal tensor component associated with **a** and **c*** is -0.56 .

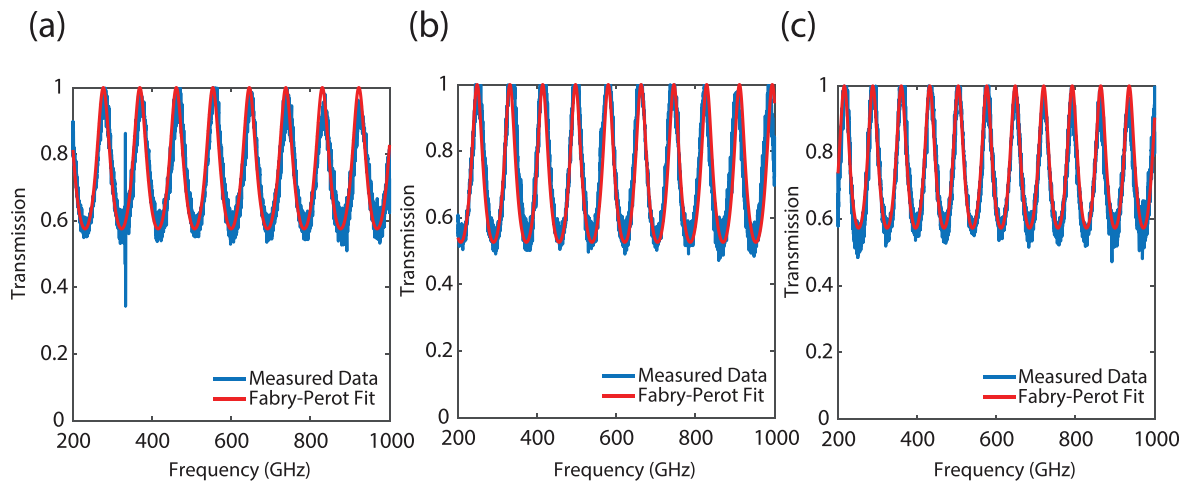


FIG. 3. Experimental (blue) and best-match calculated (red) THz-pT (polarized transmission) measured for electric field directions parallel to (a) **a***-axis [measured in sample B, (010) β -Ga₂O₃], (b) **c**-axis [measured in sample B, (010) β -Ga₂O₃], and (c) **b**-axis [measured in sample C, (001) β -Ga₂O₃]. The variation in the Fabry-Pérot fringes between spectra shown in (a) and (b) reveals the strong anisotropy between the permittivities for directions **a*** and **c**. The sample thickness for the fits in (a) and (b) was found to be 515 μ m, while that in (c) is taken to be 656 μ m.

We also include values corresponding to **a*** and **c**, which change very little and within the uncertainty limits. In Table I, it is important to note that using THz-pT measurements, we extract the dielectric permittivity values along **a***, **c**, and **b** and values for **a** and **c*** are obtained by mathematical rotation of the tensor. The knowledge of the principal directions for permittivity as reported here will be of importance for the accurate simulation of electric field distribution in electronic devices. Furthermore, our results could invariably assist subsequent investigations of terahertz conductivity of epitaxially grown conductive films (e.g., doped β -Ga₂O₃).

In conclusion, we determined the dielectric permittivity along principal lattice directions and directions perpendicular to principal planes for β -Ga₂O₃ from 200 GHz to 1 THz. In this spectral range, we do not observe any significant dispersion in the real part of the dielectric permittivity. Our results are in good agreement with recent AC capacitance and FIR-IR measurements. Our data can be used to predict the permittivity along any direction within the highly anisotropic

crystal. The data reported here will be of importance for electronic device designs and simulations involving β -Ga₂O₃.

See the [supplementary material](#) for detailed sample information, analytical models for Fabry-Pérot interference in the THz-pT data, THz-GSE of the (010) sample, and THz transmission in the a-c plane, including Refs. 30, 36, and 37.

This work was supported in part by the Air Force Office of Scientific Research under Award Nos. FA9550-18-1-0507, FA9550-18-1-0360, and FA9550-18-1-0332, by the National Science Foundation under Award Nos. DMR 1808715 and ECCS 1810096, by the National Science Foundation supported Nebraska Materials Research Science and Engineering Center under Award No. DMR 1420645, by the Swedish Governmental Agency for Innovation Systems (VINNOVA) under Competence Center Program Grant

No. 2016-05190, Swedish Research Council VR Award No. 2016-00889, and Swedish Foundation for Strategic Research Grant Nos. RIF14-055 and EM16-0024, by the Knut and Alice Wallenbergs Foundation supported grant “Wide-bandgap semiconductors for next generation quantum components,” and by the Swedish Government Strategic Research Area in Materials Science on Functional Materials at Linköping University, Faculty Grant SFO Mat LiU No. 2009-00971. This work was also partly performed in the framework of GraFOx, a Leibniz-Science Campus partially funded by the Leibniz Association, Germany. M.S. acknowledges the University of Nebraska Foundation and the J. A. Woollam Foundation for financial support. The authors thank John Blevins (Air Force Research Lab) for providing the synoptics (010) β -Ga₂O₃ bulk substrates used in the measurements.

DATA AVAILABILITY

The data that support the findings of this study are available from the corresponding author upon reasonable request.

REFERENCES

- ¹C. Janowitz, V. Scherer, M. Mohamed, A. Krapf, H. Dwelk, R. Manzke, Z. Galazka, R. Uecker, K. Irmscher, R. Fornari, M. Michling, D. Schmeißer, J. R. Weber, J. B. Varley, and C. Van de Walle, *New J. Phys.* **13**, 085014 (2011).
- ²C. Sturm, R. Schmidt-Grund, C. Kranert, J. Furthmüller, F. Bechstedt, and M. Grundmann, *Phys. Rev. B* **94**, 035148 (2016).
- ³C. Sturm, J. Furthmüller, F. Bechstedt, R. Schmidt-Grund, and M. Grundmann, *APL Mater.* **3**, 106106 (2015).
- ⁴J. Furthmüller and F. Bechstedt, *Phys. Rev. B* **93**, 115204 (2016).
- ⁵A. Mock, R. Korlacki, C. Briley, V. Darakchieva, B. Monemar, Y. Kumagai, K. Goto, M. Higashiwaki, and M. Schubert, *Phys. Rev. B* **96**, 245205 (2017).
- ⁶Z. Galazka, *Semicond. Sci. Technol.* **33**, 113001 (2018).
- ⁷J. Tsao, S. Chowdhury, M. Hollis, D. Jena, N. Johnson, K. Jones, R. Kaplar, S. Rajan, C. Van de Walle, E. Bellotti *et al.*, *Adv. Electron. Mater.* **4**, 1600501 (2018).
- ⁸M. Higashiwaki, K. Sasaki, A. Kuramata, T. Masui, and S. Yamakoshi, *Appl. Phys. Lett.* **100**, 013504 (2012).
- ⁹X. Yan, I. S. Esqueda, J. Ma, J. Tice, and H. Wang, *Appl. Phys. Lett.* **112**, 032101 (2018).
- ¹⁰S. Pearton, F. Ren, M. Tadjer, and J. Kim, *J. Appl. Phys.* **124**, 220901 (2018).
- ¹¹M. Higashiwaki, K. Sasaki, H. Murakami, Y. Kumagai, A. Koukitu, A. Kuramata, T. Masui, and S. Yamakoshi, *Semicond. Sci. Technol.* **31**, 034001 (2016).
- ¹²M. Razeghi and A. Rogalski, *J. Appl. Phys.* **79**, 7433–7473 (1996).
- ¹³X. Chen, F. Ren, S. Gu, and J. Ye, *Photonics Res.* **7**, 381–415 (2019).
- ¹⁴M. Orita, H. Ohta, M. Hirano, and H. Hosono, *Appl. Phys. Lett.* **77**, 4166–4168 (2000).
- ¹⁵A. Fiedler, R. Schewski, Z. Galazka, and K. Irmscher, *ECS J. Solid State Sci. Technol.* **8**, Q3083–Q3085 (2019).
- ¹⁶M. Schubert, R. Korlacki, S. Knight, T. Hofmann, S. Schöche, V. Darakchieva, E. Janzén, B. Monemar, D. Gogova, Q.-T. Thieu, R. Togashi, H. Murakami, Y. Kumagai, K. Goto, A. Kuramata, S. Yamakoshi, and M. Higashiwaki, *Phys. Rev. B* **93**, 125209 (2016).
- ¹⁷I. Bhaumik, R. Bhatt, S. Ganesamoorthy, A. Saxena, A. Karnal, P. Gupta, A. Sinha, and S. Deb, *Appl. Opt.* **50**, 6006–6010 (2011).
- ¹⁸T. Onuma, S. Saito, K. Sasaki, K. Goto, T. Masui, T. Yamaguchi, T. Honda, A. Kuramata, and M. Higashiwaki, *Appl. Phys. Lett.* **108**, 101904 (2016).
- ¹⁹A. Mock, R. Korlacki, S. Knight, and M. Schubert, *Phys. Rev. B* **95**, 165202 (2017).
- ²⁰A. Mock, R. Korlacki, S. Knight, and M. Schubert, *Phys. Rev. B* **97**, 165203 (2018).
- ²¹M. Schubert, A. Mock, R. Korlacki, and V. Darakchieva, *Phys. Rev. B* **99**, 041201(R) (2019).
- ²²M. Stokely, A. Mock, R. Korlacki, S. Knight, V. Darakchieva, S. Schöche, and M. Schubert, *J. Appl. Phys.* **127**, 115702 (2020).
- ²³M. Schubert, *Phys. Rev. Lett.* **117**, 215502 (2016).
- ²⁴E. Yiwen, J. Yao, and L. Wang, *Sci. Rep.* **8**, 16229 (2018).
- ²⁵K. Ghosh and U. Singiseti, *Appl. Phys. Lett.* **109**, 072102 (2016).
- ²⁶Y. Kang, K. Krishnaswamy, H. Peelaers, and C. Van de Walle, *J. Phys.* **29**, 234001 (2017).
- ²⁷S. Geller, *J. Chem. Phys.* **33**, 676 (1960).
- ²⁸H. Mueller, “Memorandum on the polarization optics of the photoelastic shutter,” Report of the OSRD Project No. OEMsr-576 2 (Massachusetts Institute of Technology, 1943).
- ²⁹M. Schubert, *Infrared Ellipsometry on Semiconductor Layer Structures: Phonons, Plasmons and Polaritons*, Springer Tracts in Modern Physics (Springer, Berlin, 2004), Vol. 209.
- ³⁰H. Fujiwara, *Spectroscopic Ellipsometry* (John Wiley & Sons, New York, 2007).
- ³¹P. Kühne, C. M. Herzinger, M. Schubert, J. A. Woollam, and T. Hofmann, *Rev. Sci. Instrum.* **85**, 071301 (2014).
- ³²M. Schubert, “Theory and application of generalized ellipsometry,” in *Handbook of Ellipsometry*, edited by E. Irene and H. Tompkins (William Andrew Publishing, 2004).
- ³³Z. Galazka, S. Ganschow, A. Fiedler, R. Bertram, D. Klimm, K. Irmscher, R. Schewski, M. Pietsch, M. Albrecht, and M. Bickermann, *J. Cryst. Growth* **486**, 82–90 (2018).
- ³⁴Z. Galazka, K. Irmscher, R. Schewski, I. M. Hanke, M. Pietsch, S. Ganschow, D. Klimm, A. Dittmar, A. Fiedler, T. Schroeder, and M. Bickermann, *J. Cryst. Growth* **529**, 125297 (2020).
- ³⁵B. Liu, M. Gu, and X. Liu, *Appl. Phys. Lett.* **91**, 172102 (2007).
- ³⁶L. Duvillaret, F. Garet, and J. L. Coutaz, “A reliable method for extraction of material parameters in terahertz time-domain spectroscopy,” *IEEE J. Sel. Top. Quantum Electron.* **2**, 739–746 (1996).
- ³⁷D. M. Pozar, *Microwave Engineering*, 3rd ed. (Wiley, Hoboken, NJ, 2005).